Check for updates

# Ultra-small Rh nanoparticles supported on $WO_{3-x}$ nanowires as efficient catalysts for visible-light-enhanced hydrogen evolution from ammonia borane†

Xiao Li, Yucong Yan, Yi Jiang, [iD] Xingqiao Wu, Shi Li, Jingbo Huang, Junjie Li, Yangfan Lin, [iD] Deren Yang and Hui Zhang [iD]*

Hydrolysis of ammonia borane (AB) is a safe and convenient means of $H_2$ production when efficient catalysts are used. Here we report a facile one-pot solvothermal method to synthesize $Rh/WO_{3-x}$ hybrid nanowires. Ultra-small Rh nanoparticles with an average size of ~1.7 nm were tightly anchored on $WO_{3-x}$ nanowires. $Rh/WO_{3-x}$ catalysts exhibited substantially enhanced activity for hydrolytic dehydrogenation of AB under both dark and visible light irradiation conditions relative to mixed Rh nanoparticles and $WO_{3-x}$ nanowires ($Rh + WO_{3-x}$), and Rh/C and $WO_{3-x}$ nanowires. X-ray photoelectron spectroscopy (XPS) analysis indicated that the synergistic effect between Rh nanoparticles and $WO_{3-x}$ nanowires was responsible for such an enhancement in activity. Specifically, $Rh/WO_{3-x}$ achieved the highest turnover frequency (TOF) with a value of 805.0 $mol_{H_2}$ $mol_{Rh}^{-1}$ $min^{-1}$ at room temperature under visible light irradiation. The $H_2$ release rate as a function of reaction time exhibited a volcano plot under visible light irradiation, indicating that a self-activation process occurred in the hydrolytic dehydrogenation of AB due to additional oxygen vacancies arising from *in situ* reduction of $WO_{3-x}$ nanowires by AB, and thus an enhanced localized surface plasmon resonance (LSPR). Such a self-activation process was responsible for the enhanced catalytic activity under visible light irradiation relative to that under dark conditions, which was supported by the lower activation energy (45.2 *vs.* 50.5 kJ $mol^{-1}$). In addition, $Rh/WO_{3-x}$ catalysts were relatively stable with only little loss in activity after five cycles due to the tight attachment between two components.

## Introduction

Hydrogen ($H_2$) has been considered as one of the best alternative energy carriers with several promising advantages including high-energy density, environmental friendliness, and rich abundance compared with traditional fossil fuels.[1–3] Based on the fuel-cell technique, it is easy to convert chemical energy of $H_2$ to electrical energy through an electrochemical process for driving electronic devices and vehicles. However, the low density of $H_2$ makes it hard to be liquefied and compressed, and thus brings about the difficulty of storage. To address this issue, it is essential to develop suitable hydrogen storage materials with secure and efficient features.[4,5] Ammonia borane (AB), as the simplest B–N compound, possesses the advantages of high hydrogen capacity (19.6 wt%), low molecular weight (30.7 g $mol^{-1}$), and high stability both in solid state and solution,

thereby making it a highly attractive candidate for the storage of hydrogen.[6–9] Generally, the hydrogen stored in AB can be released through two distinct ways: thermal dehydrogenation and hydrolysis. Compared to thermal dehydrogenation, the hydrolysis pathway is obviously more desirable due to its low energy consumption and high $H_2$ selectivity and productivity.[10–12] However, self-hydrolysis of AB is negligible at room temperature in the absence of proper catalysts. So far, lots of heterogeneous nanocatalysts consisting of noble[13–15] and non-noble metals[10,16,17] as well as their alloys[18–21] and compounds[22–24] have been developed to promote the hydrolysis of AB. Among these nanocatalysts, Rh-based catalysts have shown almost the highest activities for AB hydrolysis.[13,25–28] In view of the high cost and scarce abundance associated with Rh, massive efforts have been devoted to enhance the catalytic properties of Rh-based catalysts and maximize the utilization efficiency of Rh.

In heterogeneous catalysis, supports in a nanocatalyst might play a key role throughout the process.[27,29–32] On one hand, supports could be utilized to disperse and downsize metal nanoparticles during the synthesis, and thus expose more active

*State Key Laboratory of Silicon Materials, School of Materials Science and Engineering, Zhejiang University, Hangzhou, Zhejiang 310027, P. R. China. E-mail: msezhanghui@zju.edu.cn*

† Electronic supplementary information (ESI) available. See DOI: 10.1039/c9na00424f

sites and lead to the enhancement in catalytic performances.[15,25,26] On the other hand, coupling metal nanoparticles with supports could introduce additional synergistic effects, which intrinsically change the physical and chemical nature of the interface between them.[13,19,33–35] Therefore, the catalytic activity and selectivity could be tuned by varying different supports. As a kind of typical transition metal oxide, tungsten oxide-based materials display fascinating performances, which result from the unique feature of the outer d valence electrons.[24] Sub-stoichiometric tungsten oxides ($WO_{3-x}$) with rich oxygen vacancies have been widely investigated in various fields, such as gas sensing,[36] electrocatalysis,[37] photocatalysis,[38] electrochromism,[39] lithium-ion batteries,[40] etc. In addition, some studies show that the catalytic performances of the metal nanoparticles could be enhanced when coupling them with $WO_{3-x}$ supports.[41–43] Although there are some interesting reports about photocatalytic hydrogen evolution from AB, where other photoactive semiconductors are used to support metal nanoparticles,[44,45] there are few reports on the preparation of noble metal/$WO_{3-x}$ hybrid nanocomposites and their application in this field.

Herein, we present a simple one-pot solvothermal method to synthesize Rh/$WO_{3-x}$ hybrid nanowires. The as-obtained Rh/$WO_{3-x}$ hybrid nanocatalysts display remarkable catalytic activity for AB hydrolytic dehydrogenation in the dark with further enhancement in catalytic activity under visible light irradiation. In addition, we find an interesting self-activation process during the catalytic reaction, which might be due to additional oxygen vacancies arising from the reduction of $WO_{3-x}$ nanowires by AB.

# Experimental section

## Chemicals and materials

Rhodium(II) acetate dimer ($Rh_2(OAc)_4$, 99.99%), polyvinylpyrrolidone (PVP, $M_w \approx 29\,000$), tungsten hexacarbonyl ($W(CO)_6$, 97%), sodium hexachlororhodate(III) ($Na_3RhCl_6$) and sodium borohydride ($NaBH_4$, ≥98.0%) were purchased from Sigma-Aldrich. Tungsten chloride ($WCl_6$, 99%) and ammonia borane complex (AB, 97%) were purchased from Aladdin. Benzyl alcohol (BA, AR), ethanol (AR), and acetone (AR) were purchased from Sinopharm Chemical Reagent Co., Ltd. Deionized water (18.2 MΩ cm$^{-1}$) used in all experiments was prepared by passing through an ultra-pure purification system. All the chemicals were used as received without further purification.

## Synthesis of Rh/$WO_{3-x}$ hybrid nanowires

Rh/$WO_{3-x}$ hybrid nanowires were synthesized by a simple one-pot solvothermal method. In a standard procedure, 6 mg of $Rh_2(OAc)_4$ and 120 mg of PVP were dissolved in 10 mL of BA and stirred at room temperature for 1 h. The obtained homogeneous green solution and 100 mg of $W(CO)_6$ were transferred and sealed in a 15 mL Teflon-lined stainless steel autoclave in an Ar atmosphere. After that, the autoclave was heated at 200 °C for 12 h and cooled at room temperature after the reaction. The final product was collected by centrifugation and washed three times with ethanol and deionized water. The catalysts (denoted as Rh/$WO_{3-x}$-2) were re-dispersed in 5 mL of 10% ethanol solution and dried by freeze-drying. The loading of Rh in the catalysts was tuned by varying the amount of $Rh_2(OAc)_4$ to 3 mg (denoted as Rh/$WO_{3-x}$-1) and 12 mg (denoted as Rh/$WO_{3-x}$-3), respectively, under otherwise identical experimental conditions.

## Synthesis of Rh nanoparticles

19 mg of $Na_3RhCl_6$ and 555 mg of PVP were dissolved in 8.75 mL of deionized water. The mixture was further stirred for 30 min at 0 °C. After that, an aqueous solution of $NaBH_4$ (4.75 mg of $NaBH_4$, 1.25 mL) was rapidly injected into the mixture under vigorous stirring. Then the mixture was kept stirring for 5 min. The final product was collected by centrifugation, washed two times with acetone and ethanol, and then re-dispersed in 1 mL deionized water.

## Synthesis of $WO_{3-x}$ nanowires

$WO_{3-x}$ nanowires were synthesized according to a previous report with slight modification.[46] 150 mg of $WCl_6$ was dissolved in 10 mL of ethanol to form a transparent solution, which was then mixed with 30 mL of aqueous solution containing 250 mg of PVP in a beaker (50 mL) under vigorous stirring. After 3 min, the solution was transferred into a 50 mL Teflon-lined stainless steel autoclave. After that, the autoclave was heated at 200 °C for 4 h and cooled at room temperature after the reaction. The final product was collected by centrifugation and washed three times with ethanol.

## Characterization

Transmission electron microscopy (TEM) images were obtained with a Hitachi HT-7700 microscope operated at 100 kV. High-resolution transmission electron microscopy (HRTEM) was performed using a FEI Tecnai G2 F20 microscope operated at 200 kV. High-angle annular dark-field scanning TEM (HAADF-STEM) was conducted on an FEI Titan ChemiSTEM operated at 200 kV. X-ray powder diffraction (XRD) patterns were recorded on a Rigaku D/max-ga X-ray diffractometer with graphite monochromatic Cu Kα radiation ($\lambda = 1.54178$ Å). X-ray photoelectron spectroscopy (XPS) analysis was performed on a scanning X-ray microprobe (Axis Supra, Kratos Inc.) with Al Kα radiation. The corresponding binding energies were calibrated with a C–C 1s peak of 284.5 eV. The absorption spectra of the samples were recorded on an ultraviolet-visible-near infrared (UV-vis-NIR) spectrophotometer (Agilent, Cary 5000). Inductively coupled plasma atomic emission spectroscopy (ICP-AES) was performed using an IRIS Intrepid II XSP (TJA Co.).

## Hydrolytic dehydrogenation of AB

The catalytic reaction was carried out in a three-necked flask (25 mL) containing a stir bar connected to a gas buret. The flask was placed in a water bath at 25 °C on a magnetic stirrer under visible light irradiation ($\lambda > 400$ nm, Xe lamp equipped with

a 400 nm cutoff filter, 300 W, CEL-HXUV300, Beijing China Education Au-light Co., Ltd). In a typical procedure, 4 mL of the catalyst suspension with $6.86 \times 10^{-4}$ mmol of Rh atoms was added to the flask under magnetic stirring. The reaction was started when 1 mL of aqueous solution containing 26 mg of AB was added to the flask. In all the catalytic reactions, the atomic ratio of Rh to AB was fixed at 0.084%. The volume of $H_2$ was measured through the water-displacement method by calculating the volume of drained water. The catalytic reaction was completed when no bubble was observed. After that, another 1 mL of AB aqueous solution was further added to the flask to investigate the durability of the catalysts. This step was repeated five times. The above-mentioned reaction was also performed in the absence of the Xe lamp (defined as dark condition).

### Calculation methods

Since the Rh nanoparticles were well dispersed on supports, all the metal species in the Rh nanoparticles could be considered as active sites in the catalytic reaction. Therefore, the turnover frequency (TOF) was calculated from the equation below:

$$\text{TOF} = \frac{P_{\text{atm}} V_{\text{gas}} / RT}{n_{\text{Rh}} t}$$

where TOF is the turnover frequency, $P_{\text{atm}}$ is the atmospheric pressure (101.325 kPa), $V_{\text{gas}}$ is the volume of the generated $H_2$, $R$ is the universal gas constant (8.314 m$^3$ Pa mol$^{-1}$ K$^{-1}$), $T$ is the temperature (298 K), $n_{\text{Rh}}$ is the moles of metal species in the catalyst and $t$ is the total reaction time in minutes.

## Results and discussion

The Rh/WO$_{3-x}$ hybrid nanowires were synthesized by a simple one-pot solvothermal approach in BA containing Rh$_2$(OAc)$_4$, W(CO)$_6$, and PVP. Fig. 1 shows the morphological and structural



Fig. 1 (a) TEM image, (b) HAADF–STEM image, (c) atomic-resolution HAADF–STEM image, and (d) XRD pattern of Rh/WO$_{3-x}$-2 hybrid nanowires prepared using the standard procedure by adding 6 mg of the Rh precursor.

characterization of the sample (Rh/WO$_{3-x}$-2) prepared using the standard procedure by adding 6 mg of Rh$_2$(OAc)$_4$. From the TEM image in Fig. 1a, the sample exhibited a wire-like shape with average lengths of hundreds of nanometers and diameters of several nanometers. Careful observation shows that a rich variety of small Rh nanoparticles were anchored on the surface of the WO$_{3-x}$ nanowires to form the hybrid Rh/WO$_{3-x}$ nanostructures. Such hybrid nanowires were further confirmed by HAADF-STEM characterization, as shown in Fig. 1b. From size statistics (Fig. S1†), the average diameter of Rh nanoparticles was calculated to be ca. 1.7 nm. In addition, the WO$_{3-x}$ nanowires tended to aggregate and form bundles, leading to an uneven diameter distribution. The coalescence of the nanowires could be attributed to their intrinsic oxygen vacancies and strong interactions among individual ones.[46,47] Fig. 1c shows the atomic-resolution HAADF-STEM image of an individual hybrid nanowire, indicating a highly crystalline nature. The fringes with a lattice spacing of 0.38 nm in the nanowire can be indexed to the {010} planes of monoclinic WO$_{2.72}$ (JCPDS no. 05-0392). Such lattice fringes were perpendicular to the longitudinal axis of the nanowire, indicating that it grew along the ⟨010⟩ direction.[48] The fringes with a lattice spacing of 0.22 nm in the nanoparticle correspond to the {111} planes of face-centered cubic (fcc) Rh (JCPDS no. 05-0685). Obviously, the Rh nanoparticles were tightly anchored on the WO$_{3-x}$ nanowires, leading to a possible synergistic effect between them in the catalytic reaction. The crystal structure of these hybrid nanowires was further characterized using the XRD technique, as shown in Fig. 1d. As observed, two obvious diffraction peaks can be assigned to the (010) and (020) planes of monoclinic WO$_{2.72}$, which is consistent with the HAADF-STEM result (Fig. 1c). However, no obvious diffraction peaks associated with Rh were detected probably due to the small size of the nanoparticles and low loading of Rh. ICP-AES measurements indicated that the Rh loading in the hybrid nanowires reached approximately 1.22 wt%.

The loading of Rh in the hybrid nanowires was tuned by varying the amount of Rh$_2$(OAc)$_4$ to 3 and 12 mg. From the TEM images in Fig. S2a and c,† both samples (Rh/WO$_{3-x}$-1 and Rh/WO$_{3-x}$-3) were observed to exhibit a wire-like shape with well-dispersed nanoparticles being anchored on the surface. Obviously, the density of Rh nanoparticles on the hybrid nanowires increased with the amount of Rh precursors fed in the synthesis. The size statistics (Fig. S2b and d†) indicates that the average diameters of Rh nanoparticles in these two samples (Rh/WO$_{3-x}$-1 and Rh/WO$_{3-x}$-3) are close to 1.7 nm, which are similar to that of Rh nanoparticles in Rh/WO$_{3-x}$-2. The size of WO$_{3-x}$ nanowires was also similar in the above-mentioned three samples. In addition, ICP-AES analysis showed that the Rh loading of Rh/WO$_{3-x}$-1 and Rh/WO$_{3-x}$-3 was 0.58 wt% and 2.55 wt%, respectively.

XPS measurements were carried out to investigate the electronic interaction between Rh nanoparticles and WO$_{3-x}$ nanowires. For comparison, Rh nanoparticles (Fig. S3†) and WO$_{3-x}$ nanowires (Fig. S4†) were synthesized (see the Experimental section for details). From the TEM image in Fig. S3,† the size of Rh nanoparticles reached 1.7 nm, which was similar to that of
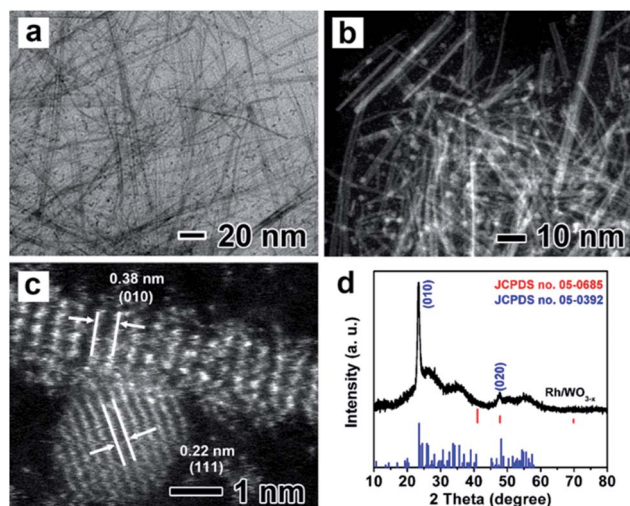
Rh nanoparticles in Rh/WO$_{3-x}$. As shown in Fig. S4,† the as-synthesized WO$_{3-x}$ nanowires were the same as those in Rh/WO$_{3-x}$ both in morphology (Fig. S4a†) and crystal structure (Fig. S4b†). After that, we simply mixed the as-prepared Rh nanoparticles with a carbon support and WO$_{3-x}$ nanowires to form Rh/C and Rh + WO$_{3-x}$ catalysts, respectively. The morphological (Fig. S5a and S6a†) and structural (Fig. S5b and S6b†) characterization indicates that Rh nanoparticles are uniformly dispersed on the supports with lattice fringes of the Rh {111} planes being clearly observed. Due to the similar structure of Rh/WO$_{3-x}$-2 to Rh/WO$_{3-x}$-1 and Rh/WO$_{3-x}$-3, only the XPS spectra of Rh/WO$_{3-x}$-2 are shown here for simplicity. Compared to the Rh 3d XPS spectrum of Rh/C, the Rh 3d peak for Rh/WO$_{3-x}$-2 shifts to a lower binding energy by 0.2 eV, as shown in Fig. 2a. However, there is almost no shift of the Rh 3d peak for Rh + WO$_{3-x}$ catalysts. This result indicates the increase in the surface electron density on Rh nanoparticles once they are coupled with WO$_{3-x}$ nanowires by direct synthesis instead of a simple mixture.[46] On the other hand, the binding energy of W 4f in Rh/WO$_{3-x}$-2 is positively shifted (Fig. 2b) compared with that of the WO$_{3-x}$ nanowires and Rh + WO$_{3-x}$, further confirming the strong electronic interactions between Rh nanoparticles and WO$_{3-x}$ nanowires in Rh/WO$_{3-x}$-2. In addition, the W 4f XPS spectra demonstrated that W species showed two oxidation states and the W 4f peaks could be fitted into two doublets: W$^{5+}$ and W$^{6+}$ species. WO$_{3-x}$ (WO$_{2.72}$) and Rh have different work functions, which are 4.50 and 4.98 eV, respectively.[49] So when Rh nanoparticles were coupled with WO$_{3-x}$ nanowires, electrons would transfer from WO$_{3-x}$ to Rh, leading to a negative charge state on Rh nanoparticles. Therefore, such an electron-rich state will benefit the electron transfer from Rh to the antibonding orbital of H$_2$O molecules, and thus accelerate hydrolytic dehydrogenation of AB by forming activated transition state complexes.[50]

Rh/WO$_{3-x}$ hybrid nanowires with different Rh loadings were then evaluated as catalysts for hydrolytic dehydrogenation of AB with WO$_{3-x}$ nanowires, Rh + WO$_{3-x}$ and Rh/C as the references. Rh/WO$_{3-x}$-1, Rh/WO$_{3-x}$-2 and Rh/WO$_{3-x}$-3 were initially tested for the hydrolysis of AB under dark conditions. As shown in Fig. S7,† these three catalysts exhibited high catalytic activities for the dehydrogenation of AB with a similar TOF approaching 500 mol$_{H_2}$ mol$_{Rh}^{-1}$ min$^{-1}$. This result could be attributed to the

same amount of Rh being involved in the catalytic reaction. So we chose Rh/WO$_{3-x}$-2 with an appropriate Rh loading as the representative example for the following research on the catalytic properties and then we called it Rh/WO$_{3-x}$ for simplification. Fig. 3 shows a comparison of the catalytic properties of Rh/WO$_{3-x}$, Rh + WO$_{3-x}$, Rh/C, and WO$_{3-x}$ nanowires in the dark and under visible light irradiation ($\lambda > 400$ nm), respectively. Obviously, WO$_{3-x}$ nanowires were inactive for the dehydrogenation of AB under both conditions. As can be seen from Fig. 3a and c, Rh/WO$_{3-x}$ exhibited a much rapider H$_2$ release rate and higher TOF value compared to those of Rh + WO$_{3-x}$ and Rh/C in the dark, implying higher activity for hydrolytic dehydrogenation of AB. Simultaneously, the total amount of produced H$_2$ for Rh/WO$_{3-x}$ was ~3.0 equivalent per mole of AB added, suggesting complete H$_2$ conversion in the catalytic reaction. However, the dehydrogenation of AB catalyzed by Rh + WO$_{3-x}$ or Rh/C was incomplete since the amount of produced H$_2$ was less than ~3.0 equivalent per mole of AB. The incomplete dehydrogenation may arise from B-containing species poisoning during the catalytic process. According to XPS analysis (Fig. 2), Rh nanoparticles would be negatively charged in Rh/WO$_{3-x}$ compared with those in Rh/C and Rh + WO$_{3-x}$. Such an electron-rich state not only accelerates the formation of activated transition state complexes, but also may promote the desorption of BO$^{2-}$ anions that were often regarded as poisoning active sites.[51] However, Rh nanoparticles in Rh/C and Rh + WO$_{3-x}$ are vulnerable to BO$^{2-}$ anions, which may cause incomplete dehydrogenation.

It is well-known that the photocatalytic efficiency is highly related to light absorption of catalysts. As such, the UV-vis-NIR absorption spectra of Rh/WO$_{3-x}$ and WO$_{3-x}$ nanowires were measured and are shown in Fig. S8.† In addition to strong valence-to-conduction band transition absorption in the UV
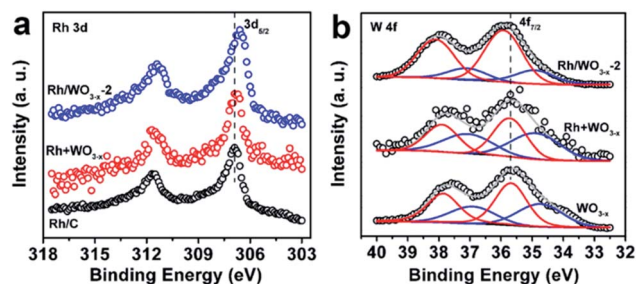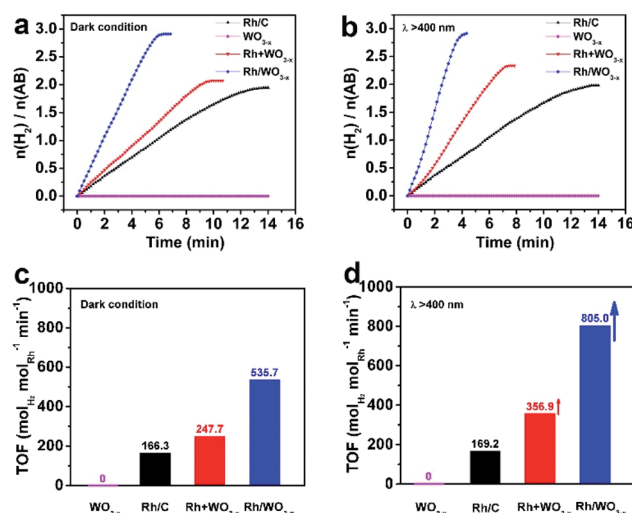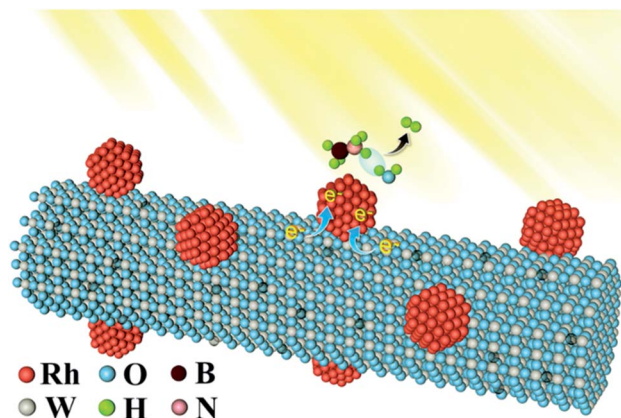


Fig. 3 Plots of time versus volume of hydrogen generated from the catalytic hydrolysis of AB over different catalysts including Rh/WO$_{3-x}$, Rh + WO$_{3-x}$, Rh/C, and WO$_{3-x}$ nanowires (a) in the dark and (b) under visible light irradiation at a reaction temperature of 298 K. Their corresponding TOF values achieved (c) in the dark and (d) under visible light irradiation.



Fig. 2 XPS spectra of (a) Rh 3d orbitals for Rh/C, Rh + WO$_{3-x}$, and Rh/WO$_{3-x}$-2 catalysts and (b) W 4f orbitals for WO$_{3-x}$ nanowires, Rh + WO$_{3-x}$, and Rh/WO$_{3-x}$-2 catalysts.

region, $WO_{3-x}$ nanowires also showed broad absorption in the visible and near infrared regions due to the presence of oxygen vacancies in the crystal structure.[52,53] After deposition of Rh nanoparticles, $Rh/WO_{3-x}$ still exhibited strong adsorption in the detected regions, especially in the UV and visible regions due to localized surface plasmon resonance (LSPR) associated with Rh nanoparticles and $WO_{3-x}$ nanowires as well as strong coupling between them. This distinct adsorption feature endowed $Rh/WO_{3-x}$ with possibly enhanced catalytic properties for hydrolytic dehydrogenation of AB with the help of visible light irradiation. Fig. 3b shows $H_2$ generation from the hydrolysis of AB catalyzed by such catalysts as a function of reaction time under visible light irradiation. It can be seen that $Rh/WO_{3-x}$ still showed a much higher $H_2$ release rate compared to $Rh + WO_{3-x}$ and Rh/C. Interestingly, both $Rh/WO_{3-x}$ and $Rh + WO_{3-x}$ displayed improved catalytic activities for hydrolytic dehydrogenation of AB under visible light irradiation relative to that under dark conditions. However, there was no obvious enhancement by using Rh/C as catalysts in the absence of $WO_{3-x}$, indicating the important role of $WO_{3-x}$ in photo-assisted hydrolytic dehydrogenation of AB. Specifically, the TOF value of $Rh/WO_{3-x}$ under visible light irradiation reached 805.0 $mol_{H_2} \, mol_{Rh}^{-1} \, min^{-1}$, which is remarkably higher than that of $Rh + WO_{3-x}$ (356.9 $mol_{H_2} \, mol_{Rh}^{-1} \, min^{-1}$) and Rh/C (169.2 $mol_{H_2} \, mol_{Rh}^{-1} \, min^{-1}$).

The temperature-dependent reaction kinetics for hydrolytic dehydrogenation of AB catalyzed by $Rh/WO_{3-x}$ was further investigated in the range of 298–328 K under dark conditions and visible light irradiation, as shown in Fig. S9a and c,† respectively. Clearly, the hydrogen generation rate increased with the reaction temperature under both conditions. Fig. S9b and d† display the corresponding Arrhenius plots of ln TOF *vs.* $1/T$, from which the activation energy $E_a$ could be calculated to be 50.5 kJ $mol^{-1}$ in the dark and 45.2 kJ $mol^{-1}$ under visible light irradiation, respectively. This decrease in $E_a$ under visible light irradiation suggested that visible light irradiation might provide a favorable transition state with a lower energy barrier. To further understand the enhancement in the photocatalytic activities of the catalysts, the dependence of the light intensity on the catalytic $H_2$ evolution was investigated. We adjusted the power of the Xe lamp from 33.3% to 66.7% and 100%. The results showed that increasing the light intensity led to an increase in the $H_2$ evolution rate of AB and the corresponding TOF values (Fig. S10a and b†). These results indicated that more photogenerated electrons were excited from $WO_{3-x}$ nanowires under visible-light irradiation with a higher intensity and then injected into Rh nanoparticles, which resulted in the enhanced electron density of the supported Rh nanoparticles and the corresponding enhanced catalytic activities. Scheme 1 shows the possible reaction mechanism for the enhancement in catalytic activity towards AB hydrolytic dehydrogenation under visible light irradiation. When visible light is used to irradiate $Rh/WO_{3-x}$ catalysts, the $WO_{3-x}$ nanowires would generate hot electrons through LSPR. Thanks to the tight attachment of Rh nanoparticles to $WO_{3-x}$ nanowires, the hot electrons would rapidly transfer to the Rh nanoparticles through the interface between them. Lots of new discrete energy levels below the



**Scheme 1** Schematic illustration of the $Rh/WO_{3-x}$ hybrid nanowire catalysts for visible-light-enhanced hydrogen evolution.

conduction band of $WO_{3-x}$ semiconductor nanowires were generated by the introduction of oxygen vacancies,[54] and metallic Rh nanoparticles were the electron trapping centers, which effectively decreased the recombination of hot electrons. As such, visible light irradiation could bring more electrons to the surface of Rh nanoparticles, and thus facilitate hydrolytic dehydrogenation of AB.

Interestingly, we noticed that the color of the $Rh/WO_{3-x}$ suspension changed from yellow-green to dark blue during the hydrolytic dehydrogenation of AB (Fig. S11a and b†). After the catalytic reaction finished, the color of the $Rh/WO_{3-x}$ suspension would remain dark blue if the flask was kept sealed. Once the $Rh/WO_{3-x}$ suspension was exposed to the air for a little while, its color would turn back to yellow-green quickly, as shown in Fig. S11c.† According to a previous report,[55] the color of substoichiometric $WO_{3-x}$ gradually turned more blue with the increase of oxygen vacancies. As such, we can speculate that $WO_{3-x}$ nanowires might be *in situ* reduced by AB during the hydrolytic dehydrogenation, leading to the increase in oxygen vacancies. In addition, the differential of the $H_2$ production volume V to $H_2$ generation time $t$ ($dV/dt$) was calculated and the corresponding plot of $dV/dt$ *vs.* $t$ is shown in Fig. S12.† In this plot, $dV/dt$ can be considered as the $H_2$ release rate. As observed, the $H_2$ release rate remains stable for the first few minutes and then gradually decreases under dark conditions, which can be attributed to the decrease in the concentration of AB over reaction time. Upon visible light irradiation, however, the $H_2$ release rate rises first and then falls, showing a volcano plot. This result indicates that a self-activation process occurred during hydrolytic dehydrogenation of AB only under visible light irradiation. The color change of the $Rh/WO_{3-x}$ suspension demonstrated the generation of additional oxygen vacancies during the catalytic reaction, leading to the formation of more discrete energy levels below the conduction band of $WO_{3-x}$ and thus the enhanced LSPR intensity.[56,57] As such, much more hot electrons were generated from LSPR under visible light irradiation, and then injected into tightly coupled Rh nanoparticles. Such additional hot electrons further facilitated the hydrolytic dehydrogenation of AB, causing the self-activation process.
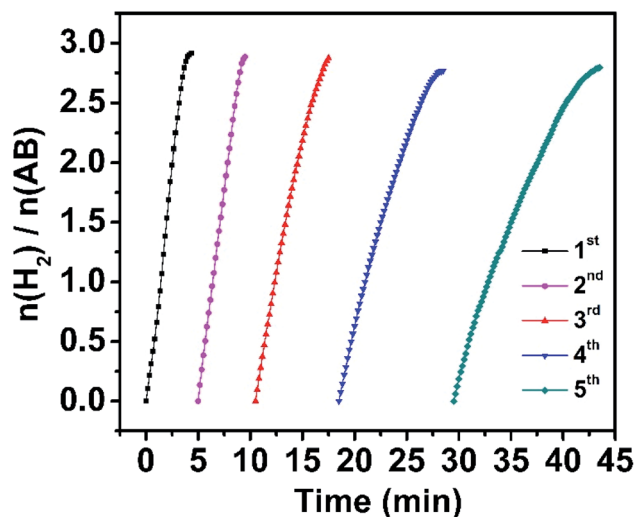
**Fig. 4** Plots of time *versus* volume of hydrogen generated from the hydrolysis of AB catalyzed by Rh/WO$_{3-x}$ for five cycles.

The stability of the Rh/WO$_{3-x}$ catalyst was also evaluated since it is another critical parameter for practical application. Reusability tests were conducted under visible light irradiation at room temperature by continuous addition of a new proportion of AB aqueous solution when the previous run was completed. As shown in Fig. 4, the catalyst can be reused at least five times and the total time for completing the hydrolytic dehydrogenation of AB gradually increases slightly. Then we further prolonged the reusability tests to ten times, and the corresponding time *vs.* volume plots and TOF values of each cycle are shown in Fig. S13a and b.† After five cycles, the Rh/WO$_{3-x}$ catalysts retain 29.7% of the initial TOF value, which is similar to a previous report,[13] but only 19.1% of the initial TOF value was retained after ten cycles. There are some possible reasons for such a decrease in the activity during cycling: (1) reactants were diluted in solution with the increase of the cycling number, (2) the viscidity of the solution also increased with the number of cycles,[58] and (3) the catalyst surface was covered with the hydrolysis product metaborate that had the deactivation effect.[29,51] In addition, the catalyst was characterized after the fifth run by TEM (Fig. S14a†) and XRD (Fig. S15a†), showing unchanged morphology and phase of the catalyst. The corresponding size distribution of Rh nanoparticles (Fig. S14b†) indicated the slight increase of their size with the number of cycles. XPS analysis (Fig. S15b†) showed that the Rh 3d peak shifts to a higher binding energy by 0.1 eV after the fifth run, which indicated the decrease in the surface electrons on Rh nanoparticles and weakness of the interaction between Rh nanoparticles and WO$_{3-x}$. It might be part of the reasons for activity degradation.

## Conclusions

In summary, we have successfully synthesized Rh/WO$_{3-x}$ hybrid nanowires by a one-pot solvothermal method, in which ultra-small Rh nanoparticles were tightly anchored on WO$_{3-x}$ nanowires. Thanks to the synergistic effect between Rh nanoparticles and WO$_{3-x}$ nanowires, Rh/WO$_{3-x}$ catalysts exhibited substantially enhanced activity for hydrolytic dehydrogenation of AB under dark conditions compared to Rh + WO$_{3-x}$, Rh/C and WO$_{3-x}$ nanowires. Benefiting from the excellent visible-light harvesting ability of the WO$_{3-x}$ nanowires, the activity of Rh/WO$_{3-x}$ catalysts was further improved with a TOF as high as 805.0 mol$_{H_2}$ mol$_{Rh}^{-1}$ min$^{-1}$ and an apparent activation energy of 45.2 kJ mol$^{-1}$. In addition, an interesting self-activation process was observed during the hydrolytic dehydrogenation of AB under visible light irradiation, which can be attributed to additional oxygen vacancies arising from *in situ* reduction of WO$_{3-x}$ nanowires by AB. Rh/WO$_{3-x}$ catalysts were also relatively stable with only little loss in activity after five cycles due to the tight hybrid nanostructures. This work offers a promising strategy to design highly efficient heterogeneous metal-oxide photocatalysts for AB hydrolytic dehydrogenation.

## Conflicts of interest

There are no conflict to declare.

## Acknowledgements

## Notes and references

1 L. Schlapbach and A. Züttel, *Nature*, 2001, **414**, 353–358.
2 M. Dresselhaus and I. Thomas, *Nature*, 2001, **414**, 332–337.
3 J. Turner, *Science*, 1999, **285**, 687–689.
4 L. Schlapbach, *Nature*, 2009, **460**, 809–811.
5 Q. Zhu and Q. Xu, *Energy Environ. Sci.*, 2015, **8**, 478–512.
6 A. Gutowska, L. Li, Y. Shin, C. Wang, X. Li, J. Linehan, R. Smith, B. Kay, B. Schmid, W. Shaw, M. Gutowski and T. Autrey, *Angew. Chem., Int. Ed.*, 2005, **44**, 3578–3582.
7 Z. Xiong, C. Yong, G. Wu, P. Chen, W. Shaw, A. Karkamkar, T. Autrey, M. Jones, S. Johnson, P. Edwards and W. David, *Nat. Mater.*, 2008, **7**, 138–141.
8 C. Hamilton, R. Baker, A. Staubitz and I. Manners, *Chem. Soc. Rev.*, 2009, **38**, 279–293.
9 W. Zhan, Q. Zhu and Q. Xu, *ACS Catal.*, 2016, **6**, 6892–6905.
10 Ö. Metin, V. Mazumder, S. Özkar and S. Sun, *J. Am. Chem. Soc.*, 2010, **132**, 1468–1469.
11 M. Yadav and Q. Xu, *Energy Environ. Sci.*, 2012, **5**, 9698–9725.
12 U. Demirci and P. Miele, *Energy Environ. Sci.*, 2011, **4**, 3334–3341.
13 S. Akbayrak, Y. Tonbul and S. Özkar, *Appl. Catal., B*, 2016, **198**, 162–170.
14 M. Chandra and Q. Xu, *J. Power Sources*, 2007, **168**, 135–142.
15 L. Zhang, Y. Wang, J. Li, X. Ren, H. Lv, X. Su, Y. Hu, D. Xu and B. Liu, *ChemCatChem*, 2018, **10**, 1–8.

16 J. Yan, X. Zhang, S. Han, H. Shioyama and Q. Xu, *Angew. Chem., Int. Ed.*, 2008, **47**, 2287–2289.

17 M. Shen, H. Liu, C. Yu, Z. Yin, M. Muzzio, J. Li, Z. Xi, Y. Yu and S. Sun, *J. Am. Chem. Soc.*, 2018, **140**, 16460–16463.

18 F. Fu, C. Wang, Q. Wang, A. Martinez-Villacorta, A. Escobar, H. Chong, X. Wang, S. Moya, L. Salmon, E. Fouquet, J. Ruiz and D. Astruc, *J. Am. Chem. Soc.*, 2018, **140**, 10034–10042.

19 K. Mori, K. Miyawaki and H. Yamashita, *ACS Catal.*, 2016, **6**, 3128–3135.

20 Q. Wang, F. Fu, S. Yang, M. Moro, M. Ramirez, S. Moya, L. Salmon, J. Ruiz and D. Astruc, *ACS Catal.*, 2019, **9**, 1110–1119.

21 H. Zhang, X. Gu, P. Liu, J. Song, J. Cheng and H. Su, *J. Mater. Chem. A*, 2017, **5**, 2288–2296.

22 C. Peng, L. Kang, S. Cao, Y. Chen, Z. Lin and W. Fu, *Angew. Chem., Int. Ed.*, 2015, **54**, 15725–15729.

23 C. Hou, Q. Li, C. Wang, C. Peng, Q. Chen, H. Ye, W. Fu, C. Che, N. López and Y. Chen, *Energy Environ. Sci.*, 2017, **10**, 1770–1776.

24 Y. Lou, J. He, G. Liu, S. Qi, L. Cheng, J. Chen, Y. Zhao and J. Zhu, *Chem. Commun.*, 2018, **54**, 6188–6191.

25 Q. Yao, Z. Lu, Y. Jia, X. Chen and X. Liu, *Int. J. Hydrogen Energy*, 2015, **40**, 2207–2215.

26 R. Lu, M. Hu, C. Xu, Y. Wang, Y. Zhang, B. Xu, D. Gao, J. Bi and G. Fan, *Int. J. Hydrogen Energy*, 2018, **43**, 7038–7045.

27 L. Wang, H. Li, W. Zhang, X. Zhao, J. Qiu, A. Li, X. Zheng, Z. Hu, R. Si and J. Zeng, *Angew. Chem., Int. Ed.*, 2017, **56**, 4712–4718.

28 H. Zou, B. Jin, R. Wang, Y. Wu, H. Yang and S. Qiu, *J. Mater. Chem. A*, 2018, **6**, 24166–24174.

29 Q. Zhu, J. Li and Q. Xu, *J. Am. Chem. Soc.*, 2013, **135**, 10210–10213.

30 J. S. Du, T. Bian, J. Yu, Y. Jiang, X. Wang, Y. Yan, Y. Jiang, C. Jin, H. Zhang and D. Yang, *Adv. Sci.*, 2017, **4**, 1700056.

31 Y. Jiang, X. Wu, Y. Yan, S. Luo, X. Li, J. Huang, H. Zhang and D. Yang, *Small*, 2019, **15**, 1805474.

32 Y. Jiang, Y. Yan, Y. Han, H. Zhang and D. Yang, *RSC Adv.*, 2017, **7**, 43373–43379.

33 Q. Yao, Z. Lu, Y. Yang, Y. Chen, X. Chen and H. Jiang, *Nano Res.*, 2018, **11**, 4412–4422.

34 M. Khalily, H. Eren, S. Akbayrak, H. Susapto, N. Biyikli, S. Özkar and M. Guler, *Angew. Chem., Int. Ed.*, 2016, **55**, 12257–12261.

35 Y. Ge, W. Ye, Z. H. Shah, X. Lin, R. Lu and S. Zhang, *ACS Appl. Mater. Interfaces*, 2017, **9**, 3749–3756.

36 A. Ponzoni, E. Comini, G. Sberveglieri, J. Zhou, S. Deng, N. Xu, Y. Ding and Z. Wang, *Appl. Phys. Lett.*, 2006, **88**, 203101.

37 T. Zheng, W. Sang, Z. He, Q. Wei, B. Chen, H. Li, C. Cao, R. Huang, X. Yan, B. Pan, S. Zhou and J. Zeng, *Nano Lett.*, 2017, **17**, 7968–7973.

38 J. Liu, O. Margeat, W. Dachraoui, X. Liu, M. Fahlman and J. Ackermann, *Adv. Funct. Mater.*, 2014, **24**, 6029–6037.

39 J. Liu, J. Zheng, J. Wang, J. Xu, H. Li and S. Yu, *Nano Lett.*, 2013, **13**, 3589–3593.

40 K. Bao, W. Mao, G. Liu, L. Ye, H. Xie, S. Ji, D. Wang, C. Chen and Y. Li, *Nano Res.*, 2017, **10**, 1903–1911.

41 Z. Xi, D. Erdosy, A. Mendoza-Garcia, P. Duchesne, J. Li, M. Muzzio, Q. Li, P. Zhang and S. Sun, *Nano Lett.*, 2017, **17**, 2727–2731.

42 Y. Lu, Y. Jiang, X. Gao, X. Wang and W. Chen, *J. Am. Chem. Soc.*, 2014, **136**, 11687–11697.

43 F. Li, H. Gong, Y. Wang, H. Zhang, Y. Wang, S. Liu, S. Wang and C. Sun, *J. Mater. Chem. A*, 2014, **2**, 20154–20163.

44 J. Song, X. Gu, J. Cheng, N. Fan, H. Zhang and H. Su, *Appl. Catal., B*, 2018, **225**, 424–432.

45 J. Song, X. Gu, Y. Cao and H. Zhang, *J. Mater. Chem. A*, 2019, **7**, 10543–10551.

46 H. Zhang, C. Huang, R. Tao, Y. Zhao, S. Chen, Z. Sun and Z. Liu, *J. Mater. Chem.*, 2012, **22**, 3354–3359.

47 X. Lou and H. Zeng, *Inorg. Chem.*, 2003, **42**, 6169–6171.

48 G. Xi, S. Ouyang, P. Li, J. Ye, Q. Ma, N. Su, H. Bai and C. Wang, *Angew. Chem., Int. Ed.*, 2012, **51**, 2395–2399.

49 F. Liu, F. Mo, S. Jin, L. Li, Z. Chen, R. Sun, J. Chen, S. Deng and N. Xu, *Nanoscale*, 2011, **3**, 1850–1854.

50 Z. Li, T. He, L. Liu, W. Chen, M. Zhang, G. Wu and P. Chen, *Chem. Sci.*, 2017, **8**, 781–788.

51 W. Chen, J. Ji, X. Feng, X. Duan, G. Qian, P. Li, X. Zhou, D. Chen and W. Yuan, *J. Am. Chem. Soc.*, 2014, **136**, 16736–16739.

52 Y. Zhang, Y. Shi, R. Chen, L. Tao, C. Xie, D. Liu, D. Yan and S. Wang, *J. Mater. Chem. A*, 2018, **6**, 23028–23033.

53 F. Lei, Y. Sun, K. Liu, S. Gao, L. Liang, B. Pan and Y. Xie, *J. Am. Chem. Soc.*, 2014, **136**, 6826–6829.

54 J. Yan, T. Wang, G. Wu, W. Dai, N. Guan, L. Li and J. Gong, *Adv. Mater.*, 2015, **27**, 1580–1586.

55 G. Wang, Y. Ling, H. Wang, X. Yang, C. Wang, J. Zhang and Y. Li, *Energy Environ. Sci.*, 2012, **5**, 6180–6187.

56 H. Bai, W. Yi, J. Liu, Q. Lv, Q. Zhang, Q. Ma, H. Yang and G. Xi, *Nanoscale*, 2016, **8**, 13545–13551.

57 K. Manthiram and A. Alivisatos, *J. Am. Chem. Soc.*, 2012, **134**, 3995–3998.

58 U. Sanyal, U. Demirci, B. Jagirdar and P. Miele, *ChemSusChem*, 2011, **4**, 1731–1739.